A simple model for interpreting temperature variability and its higher-order changes

Article

Published Version

Open access

It is advisable to refer to the publisher's version if you intend to cite from the work. See Guidance on citing.

www.reading.ac.uk/centaur

CentAUR

Central Archive at the University of Reading

Reading's research outputs online

A Simple Model for Interpreting Temperature Variability and Its Higher-Order Changes⌗

TALIA TAMARIN-BRODSKY,[a,b] KEVIN HODGES,[a,c] BRIAN J. HOSKINS,[a] AND THEODORE G. SHEPHERD[a]

[a] *Department of Meteorology, University of Reading, Reading, United Kingdom*
[b] *Department of Geophysics, Tel-Aviv University, Tel Aviv, Israel*
[c] *National Centre for Atmospheric Science, University of Reading, Reading, United Kingdom*

ABSTRACT: Atmospheric temperature distributions are often identified with their variance, while the higher-order moments receive less attention. This can be especially misleading for extremes, which are associated with the tails of the probability density functions (PDFs), and thus depend strongly on the higher-order moments. For example, skewness is related to the asymmetry between positive and negative anomalies, while kurtosis is indicative of the "extremity" of the tails. Here we show that for near-surface atmospheric temperature, an approximate linear relationship exists between kurtosis and skewness squared. We present a simple model describing this relationship, where the total PDF is written as the sum of three Gaussians, representing small deviations from the climatological mean together with the larger-amplitude cold and warm temperature anomalies associated with synoptic systems. This model recovers the PDF structure in different regions of the world, as well as its projected response to climate change, giving a simple physical interpretation of the higher-order temperature variability changes. The kurtosis changes are found to be largely predicted by the skewness changes. Building a deeper understanding of what controls the higher-order moments of the temperature variability is crucial for understanding extreme temperature events and how they respond to climate change.

KEYWORDS: Advection; Asymmetry; Climate change; Temperature; Idealized models
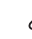
1. Introduction

Extreme temperature events such as heat waves and cold spells can present a serious threat to humans, livestock, and agricultural production (Bindoff et al. 2013; Field et al. 2012). Assessing the impact of a changing climate on temperature extremes remains a key challenge, and much work is still needed in order to provide reliable predictions of changes in their frequency, intensity, and persistence. While climate models robustly agree that the mean surface temperature is projected to increase due to anthropogenic warming, the higher-order temperature variability changes are less certain (e.g., Tamarin-Brodsky et al. 2020). The latter are especially important for temperature extremes, which lie in the tails of the probability density functions (PDFs).

Much effort in recent years has been directed to studying the mean temperature and temperature variance response to climate change (Schär et al. 2004; Screen 2014; Fischer and Schär 2009; Volodin and Yurova 2013; Parey et al. 2013; Kodra and Ganguly 2014; Schneider et al. 2015; Gao et al. 2015; Holmes et al. 2016; Bathiany et al. 2018; Dai and Deng 2021; Xu et al. 2020). It is now generally acknowledged that the temperature variance is projected to decrease in the Northern Hemisphere (NH) during winter under greenhouse gas warming, due to the excess warming of the Arctic region and associated decrease in the meridional (equator-to-pole) temperature gradient (Screen 2014; Schneider et al. 2015; Tamarin-Brodsky et al. 2020). The basic idea behind the variance decrease, proposed by Screen (2014) and then formulated by Schneider et al. (2015), can be understood by relating the temperature fluctuations, through linear meridional advection, to the meridional background temperature gradient. For example, if the meridional background temperature is uniform everywhere (zero gradient), then no temperature perturbation is generated by advection of air between the tropics and the pole. Similarly, a weakening of the meridional temperature gradient will be associated with a weakening of the temperature anomalies (and thus a decrease in the temperature variance), all else being equal.

Recently, there has been a growing interest in understanding the higher-order moments of the temperature variability, due to their importance for temperature extremes. Specifically, many recent studies have highlighted the importance of skewness [$S = \overline{T'^3}/(\overline{T'^2})^{3/2}$, the third-order moment of the temperature PDF], which relates to the asymmetry between the cold and warm temperature anomalies, for capturing correctly the temperature distributions and their response to climate change (Petoukhov et al. 2008; Fischer and Schär 2009; Ruff and Neelin 2012; Perron and Sura 2013; Kodra and Ganguly 2014; Sardeshmukh et al. 2015; Garfinkel and Harnik 2017; Linz et al. 2018; Loikith and Neelin 2019; Tamarin-Brodsky et al. 2019; Linz et al. 2020; Tamarin-Brodsky et al. 2020). A zero skewness implies that the positive and negative tails are symmetric around the mean (e.g., Figs. 1a,b), while a positive skewness implies that the positive tail is longer than the negative tail (e.g., Figs. 1c,d) (with the
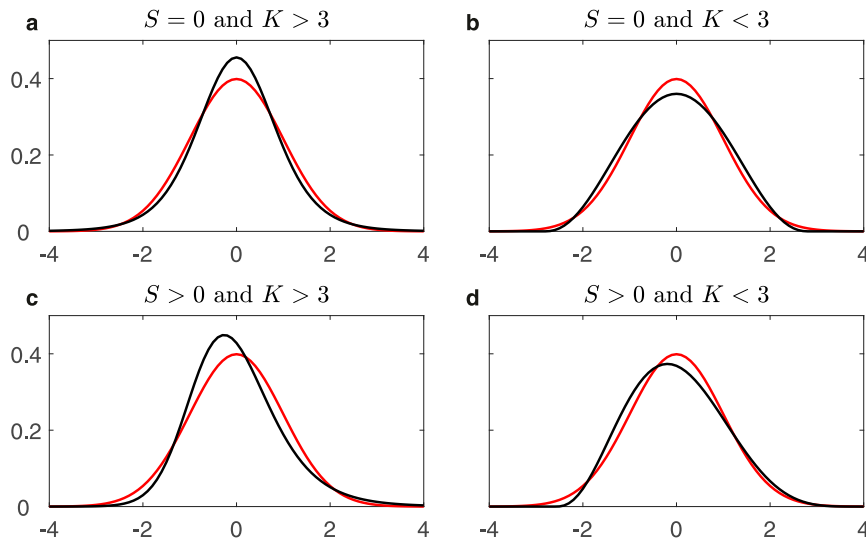

Fig. 1. An illustration of PDFs with different kurtosis and skewness values. A PDF with (a) positive excess kurtosis ($K - 3 > 0$) and zero skewness ($S = 0$) (black), (b) negative excess kurtosis ($K - 3 < 0$) and zero skewness ($S = 0$) (black), (c) positive excess kurtosis ($K - 3 > 0$) and positive skewness ($S > 0$) (black), and (d) negative excess kurtosis ($K - 3 < 0$) and positive skewness ($S > 0$) (black). In all panels, a Gaussian PDF ($S = 0$ and $K = 3$) is shown in red for reference.

opposite for negative skewness). Two main mechanisms have been proposed to understand how temperature skewness can be generated dynamically, through meridional advection. The first involves nonlinear meridional advection of temperature anomalies by anomalous cyclone–anticyclone pairs that are responsible for the equatorward (poleward) movement of the cold (warm) temperature anomalies (Garfinkel and Harnik 2017; Linz et al. 2018; Tamarin-Brodsky et al. 2019). This gives rise to the dipole skewness structure seen in the midlatitude storm track regions, which is most pronounced in the Southern Hemisphere (SH) storm tracks (see Fig. 2a). The second mechanism involves linear meridional advection of temperature anomalies generated by spatially asymmetric background temperature gradients (Tamarin-Brodsky et al. 2020) and is mostly important in the NH due to

the abundance of continents that create strong temperature gradients. There is strong evidence that a positive skewness change is projected to occur over most of the NH during winter (Gao et al. 2015; Tamarin-Brodsky et al. 2020), indicating that the cold anomalies weaken more strongly than the warm anomalies (relative to the already warmer mean temperatures). This occurs because the largest gradient decreases, which are due to Arctic amplification, occur closer to the pole. Hence, cold anomalies advected from the Arctic weaken significantly more than warm anomalies advected from the tropics (Tamarin-Brodsky et al. 2020).

Kurtosis, on the other hand, has been studied much less. Kurtosis [$K = \overline{T'^4}/\left(\overline{T'^2}\right)^2$, the fourth-order moment of the temperature PDF] is indicative of the "extremity" of the tails, and is therefore especially important for extremes. The kurtosis of a
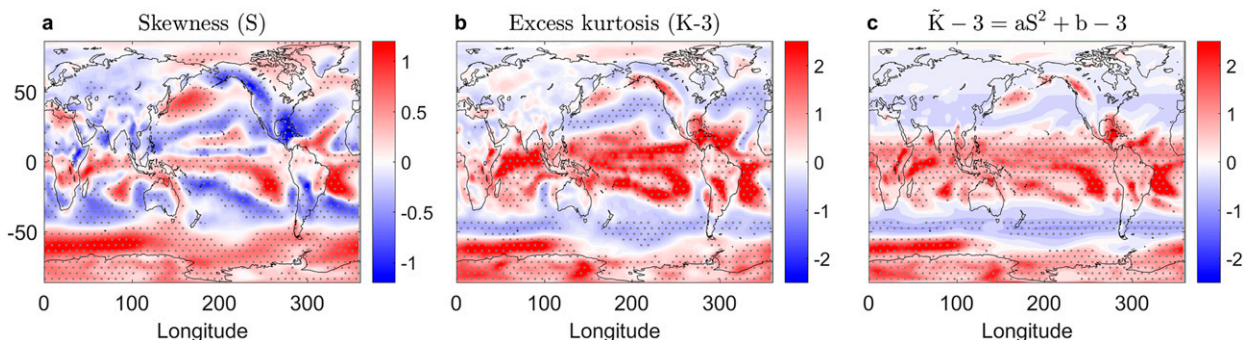

Fig. 2. The 850-hPa temperature (a) skewness and (b) excess kurtosis, based on ERA-Interim data averaged over the years 1980–2015 during December–February (DJF). (c) The estimated excess kurtosis (see text for details). Regions where the skewness and excess kurtosis values are statistically significant are stippled.

Fig(s). 1,2 live 4/C

Gaussian distribution is exactly 3 (Fig. 1, red), which is why it is often convenient to consider the excess kurtosis ($K - 3$). Positive excess kurtosis ($K > 3$) generally implies that more of the PDF lies around the mean and at the extreme tails, while less of the PDF is in the midrange (Fig. 1a). In such a PDF, extreme events occur more frequently than in a Gaussian distribution. Similarly, negative excess kurtosis ($K < 3$) implies that extreme events occur less frequently than in a Gaussian distribution (Fig. 1b). Note however that this is not necessarily true for both tails if skewness is nonzero. Figure 1c shows an example where both skewness and excess kurtosis are positive but only the positive tail is longer than a Gaussian, while the negative tail is shorter than a Gaussian. The opposite would be true for a negative skewness and positive excess kurtosis. In Fig. 1d, skewness is positive and excess kurtosis is negative, and while both tails are shorter than a Gaussian in this case, it is clear that the negative tail is significantly shorter. Hence, care must be taken with regards to extremes and preconceptions about kurtosis, when skewness is nonzero.

While some studies have included an analysis of temperature kurtosis (Perron and Sura 2013; McKinnon et al. 2016), no deeper investigation of temperature kurtosis and its projected changes has been performed, to our knowledge. The observed kurtosis structure of near-surface temperature based on re-analysis data was presented in Perron and Sura (2013), who noted that regions of large skewness values tend to collocate with large kurtosis values, but did not examine it further. McKinnon et al. (2016) analyzed observed data from weather stations to estimate the temperature distribution changes during summer, and suggested that most of the PDF changes can be explained by a shift in the mean, while the changes in the remaining variability were small. Several previous studies have found an interesting parabolic relationship between kurtosis and skewness for variables such as sea surface temperature (SST) (Sura and Sardeshmukh 2008), sea surface height (Sura and Gille 2010), vorticity and sea level in ocean jets (Hughes et al. 2010; David et al. 2017), and plasma fluids (Krommes 2008; Guszejnov et al. 2013). This remarkable parabolic relation between kurtosis and skewness is not a fundamental statistical result (i.e., it does not follow directly from the definitions of skewness and kurtosis) but has been shown to hold in several complex systems (Schopflocher and Sullivan 2005; Sattin et al. 2009; Cristelli et al. 2012).

For SSTs, Sura and Sardeshmukh (2008) have shown how a linear mixed layer model for SST with a mixture of additive (SST-independent) and multiplicative (SST-dependent) noise can account for the skewness–kurtosis parabolic relation, by writing a Fokker–Planck type equation for the stationary PDF of the SST anomalies. Alternatively, Hughes et al. (2010) explored the statistics of vorticity and sea level height in ocean jets and developed a simple model that captures the squared relationship. They considered a sharp jet, which may be approximated as a step in vorticity. At the center of the jet, there is a flip from negative to positive vorticity anomalies, as the mixing barrier meanders due to passing Rossby waves. The model describes the statistics as the sum of two Gaussians, accounting for the positive and negative anomalies, and noise is then represented by the width of the Gaussians. Despite its simplicity, the model captures the key features such as the squared relationship between skewness and kurtosis, and explains why strong jets acting as mixing barriers tend to be associated with zero skewness and a low kurtosis.

In this paper we extend the model proposed by Hughes et al. (2010). We apply it to low-level atmospheric temperature to explain the squared relationship between temperature skewness and kurtosis, and further explore how it can be used to better understand the future temperature variability changes. The two-Gaussian model used in Hughes et al. (2010) is appropriate for jets in a staircase model of two distinct well-homogenized fluids with a strong mixing barrier. Hence, we cannot expect it to work well for temperature, whose horizontal distribution in the atmosphere is not generally well represented as a staircase of homogenized temperatures. In the proposed model, the temperature PDF is written as the sum of three (rather than two) Gaussians, with two Gaussians representing the cold and warm anomalies, and another near-zero Gaussian representing small departures from the mean temperature (i.e., a Gaussian mixture model, with the choice of three Gaussians motivated by a physical rather than a statistical perspective). Note that if one assumes Gaussianity of the temperature PDF (e.g., Schneider et al. 2015), then only one Gaussian is considered around the mean. Hence, our model can be thought of as an extension of the single Gaussian, to include the effect of long-range advection associated with coherent motions (represented by the warm and cold Gaussians), as opposed to random noise (represented by the Gaussian around the mean). A similar three-Gaussian model was used in David et al. (2017) to study the statistics of turbulent barotropic ocean jets, but the analytical solutions of the three-Gaussian PDF were not explicitly written or investigated further there.

The three-Gaussian model also extends our results from a previous study (Tamarin-Brodsky et al. 2020), where simple equations were derived for temperature variance and skewness in terms of the mean intensity of cold and warm anomalies, assuming a Bernoulli distribution. The oversimplification of the Bernoulli distribution used in that study did not allow for a proper representation of kurtosis. The essential inclusion of the near-zero anomalies, as well as the introduction of noise by allowing for deviations around the mean intensities, is enough to capture the essence of the temperature variability, yet keeping the simplicity in terms of interpretation. We show how the three-Gaussian model can be useful for better understanding temperature variability and its projected changes, by relating the PDF variance, skewness, and kurtosis changes to changes in the intensity and frequency of the cold, near-zero, and warm anomalies separately.

The paper is organized as follows. The methods and data used are first described in section 2. Section 3 gives an overview of the observed temperature skewness and kurtosis and the parabolic relationship between them. In section 4, we review previous studies and extend them to develop the three-Gaussian model. We present interesting limits of the solutions to build intuition of how the model works, and present idealized examples to demonstrate the role of the different model parameters. The model is then used in section 5 to

investigate the latitudinal dependence of the parabolic relation, and its interpretation for temperature variability in the SH midlatitudes is discussed. In section 6, the usefulness of the model for interpreting future temperature variability changes is presented. A summary and discussion are given in section 7.

2. Data and methods

In this study we use the 6-hourly 850-hPa temperature field from the ECMWF interim reanalysis (herein ERAI) dataset (Dee et al. 2011) covering the period 1980–2014, where the background climatology is defined for every 6-hourly time period as its average over the 35 years in order to remove both the diurnal and the seasonal cycle. We concentrate on the NH winter season [December–February (DJF)], and on the 850-hPa level, which is mostly above the boundary layer but still highly correlated with the surface temperature (Tamarin-Brodsky et al. 2020), because the focus here is on the dynamical origin of the temperature anomalies and in winter we expect temperatures to be mostly governed by large-scale dynamics, whereas in summer other processes (such as local land surface feedbacks) may be more important (Fischer and Schär 2009).

For the projected temperature variability changes, we use the 6-hourly 850-hPa temperature field from 26 CMIP5 models (see the model list in Table S1 in the online supplemental material). We analyze the r1i1p1 ensemble member from the representative concentration pathway 8.5 (RCP8.5) emissions scenario (Taylor et al. 2012). The data cover a period of 19 years in the historical period (1981–99) and 19 years in the projected period (2081–99) during DJF. The historical simulations are forced by both the observed anthropogenic and natural atmospheric forcings, and in the projected simulations the radiative forcing increases by about 8.5 W m^{-2} by year 2100. Similar to ERAI, for each model the background climatology is defined for every 6-hourly time period as its average over the 19 years. Perturbations are defined as deviations from the 6-hourly climatology (for the historical and projected simulations separately). The skewness and kurtosis are calculated first for each model separately, and then averaged together to produce the ensemble means.

3. The observed relationship between temperature skewness and kurtosis

The spatial structure of the low-level (850 hPa) temperature skewness from ERAI data (Fig. 2a) has been presented previously in several studies (e.g., Tamarin-Brodsky et al. 2019), but is presented here for completeness. Temperature skewness is generally negative (positive) on the equatorward (poleward) flank of the midlatitude storm tracks over the oceans in both hemispheres. This is mainly due to nonlinear meridional temperature advection by anomalous cyclone–anticyclone pairs, which advect the cold (warm) temperature anomalies equatorward (poleward) in regions of strong localized meridional temperature gradients (Garfinkel and Harnik 2017; Linz et al. 2018; Tamarin-Brodsky et al. 2019). Other processes, such as linear advection of asymmetric meridional temperature

gradients (Tamarin-Brodsky et al. 2020) and regional land surface feedbacks or the vicinity to ocean and mountains (Lutsko et al. 2019; Loikith and Neelin 2019), can also influence temperature skewness.

The low-level (850 hPa) temperature excess kurtosis in ERAI (Fig. 2b) was shown in Perron and Sura (2013), but not investigated further to our knowledge. Temperature kurtosis is generally high (positive excess kurtosis) in the tropics, and a clear dipole structure can be seen in the SH midlatitude storm track region, but with a center that is farther to the south compared to the skewness dipole. Just by comparing Figs. 2a and 2b it is hard to see the parabolic relationship between kurtosis and skewness. This can be more easily seen by examining scatterplots of kurtosis versus skewness in different regions, for example, in the SH (Fig. 3a) and in the NH (Fig. 3b) midlatitudes. In the tropics (Fig. 3c), this relationship is less pronounced, as points are scattered more widely, but still apparent. Similar plots have been identified in previous studies for other variables (as discussed above), which indicates that this might be a fundamental aspect of advective fluid systems (Schopflocher and Sullivan 2005).

To get a rough idea of the coefficients of this relationship, in Figs. 3d–f the points are plotted for the same latitudinal bands, but for kurtosis (K) and skewness squared (S^2). We find that kurtosis can be estimated as $K \approx aS^2 + b$, with $a = 1.6$, 1.6, and 2.3 and $b = 2.7$, 2.8, and 3.5 for the SH midlatitudes, NH midlatitudes, and tropics, respectively. Hence, depending on the value of the skewness S, it is clear that the excess kurtosis $K - 3$ can be either negative or positive in the midlatitudes (since b is close to 3 and $b - 3 < 0$), while it is mostly positive in the tropics (since $b - 3 > 0$), as can indeed be seen from Fig. 2b.

The statistical significance of the observed skewness and excess kurtosis values can be determined using the standard errors of skewness and kurtosis, given by $\sigma_S = \sqrt{(6/N_i)}$ and $\sigma_K = \sqrt{(24/N_i)} = 2\sigma_S$, respectively, where N_i is the number of independent degrees of freedom (Brooks and Carruthers 1953). Skewness and excess kurtosis values are then considered significant at the 95% level if they are larger in magnitude than $2\sigma_S$ and $2\sigma_K$, respectively (Perron and Sura 2013). We can estimate $N_i = 450$ (90 days for a season multiplied by the 35 years and divided by a typical atmospheric decorrelation time scale of 7 days), which gives $2\sigma_S \approx 0.23$ and $2\sigma_K \approx 0.46$. Regions where skewness and excess kurtosis values are larger than these thresholds are stippled in Fig. 2 (and in Fig. 8 for the historical CMIP5 values) and denote regions where the PDFs deviate significantly from a Gaussian. It is interesting to note that temperatures over land are generally more Gaussian than temperatures over oceans, particularly over Eurasia (Fig. 2).

4. A simple model for temperature variability

In a previous study by the same authors (Tamarin-Brodsky et al. 2020), simplified expressions were derived for temperature variance and skewness in terms of the mean intensities of cold and warm temperature anomalies (see section 2 in the online supplemental material):

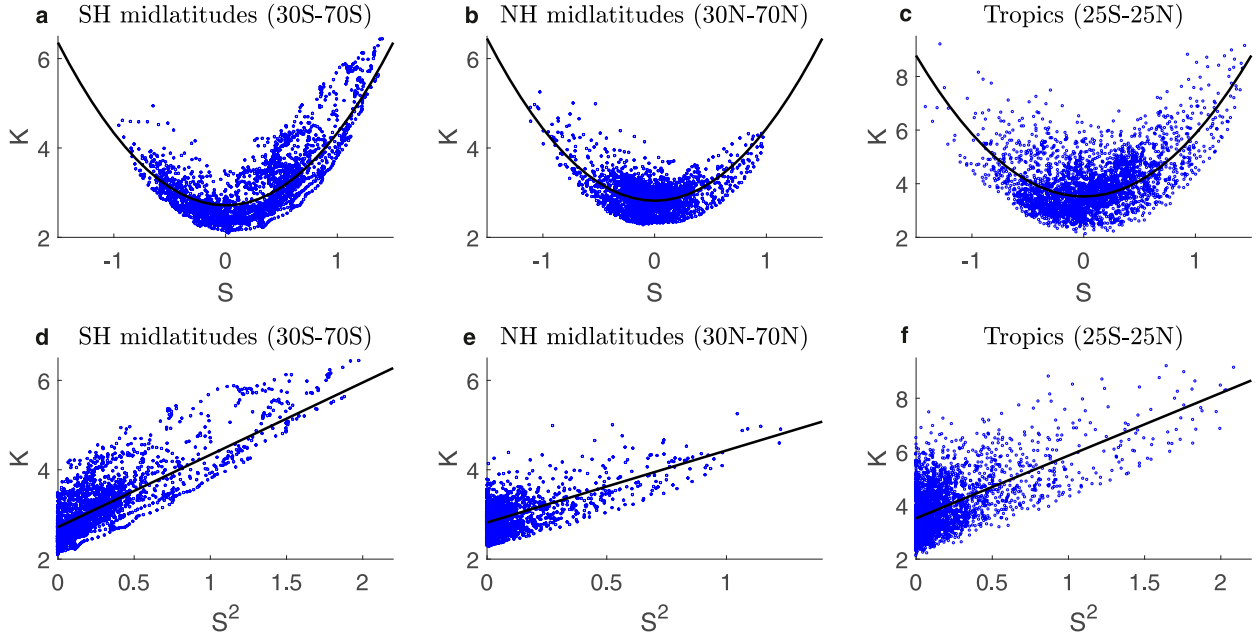$$\sigma^2 \approx T_w T_c \qquad (1)$$

FIG. 3. Scatterplots of temperature kurtosis vs skewness, based on ERA-Interim data covering the period 1980–2015 during DJF. (a)–(c) Kurtosis vs skewness is plotted for SH midlatitudes (30°–70°S), NH midlatitudes (30°–70°N), and the tropics (25°S–25°N), respectively. (d)–(f) As in (a)–(c), but for kurtosis vs skewness squared. The black lines in (a)–(c) are the best parabolic fit of the points, while in (d)–(f) a best linear fit is used.

and

$$S = \frac{(T_w - T_c)}{\sigma}, \qquad (2)$$

where $T_c = |T_c'|$ and $T_w = |T_w'|$ denote the average absolute intensity of the cold and warm temperature anomalies, respectively. To derive these equations, a Bernoulli distribution was implicitly assumed, namely that at every time step we either get a warm temperature anomaly of mean intensity T_w with probability $p_w = T_c/(T_w + T_c)$ or a cold temperature anomaly of mean intensity T_c with probability $p_c = T_w/(T_w + T_c)$, such that overall $p_w + p_c = 1$ as needed. For this simple Bernoulli approximation, it is easy to show (see section 2 in the supplemental material) that kurtosis is then directly related to skewness by

$$K = S^2 + 1. \qquad (3)$$

This is in fact the lowest possible K for a given S (Pearson 1916). If, for example, this Bernoulli distribution describes an unbiased coin toss with two states of equal probability, then $S = 0$ and $K = 1$, which is the minimum possible kurtosis (Pearson 1916).

While some of the high kurtosis regions seen in Fig. 2b are indeed captured by high values of $S^2 + 1$, this relationship is oversimplified. The excess kurtosis ($K - 3$) estimated from (3) (see supplemental Fig. S1) is negative everywhere (because the skewness squared values are smaller than 2), unlike the actual excess kurtosis shown in Fig. 2b. Hence, while the simplified skewness from the Bernoulli distribution given by (2) recovers well the actual skewness (see Fig. 2 from Tamarin-Brodsky et al. 2020), the simplified kurtosis given by (3) fails to recover

correctly the actual kurtosis (Fig. 2b). One of the main limitations of this simple approximation for studying kurtosis is the assumption that only warm or cold anomalies can occur, while ignoring the weight of the distribution around the mean.

To further study the nature of the relation between skewness and kurtosis, we consider first a slightly more complicated case of a modified Bernoulli distribution with three variables: T_w, T_c, and T_0, where the latter represents the mean with probability p_0, such that $p_w + p_c + p_0 = 1$ (here $T_0 = 0$ since the T terms are measured as anomalies relative to the mean). For this system, it is easy to show (see section 3 in the supplemental material) that the probabilities are now modified to $p_w = T_c(1 - p_0)/(T_w + T_c)$ and $p_c = T_w(1 - p_0)/(T_w + T_c)$, variance is given by $\sigma^2 = T_w T_c(1 - p_0)$, skewness by $S = (T_w - T_c)/\sqrt{T_w T_c(1 - p_0)}$, and kurtosis by

$$K = S^2 + \frac{1}{(1 - p_0)}. \qquad (4)$$

For $p_0 = 0$, one recovers the earlier Bernoulli results given in (3). For large p_0 values (approaching one), Eq. (4) predicts high kurtosis (which can explain the high kurtosis values found in the tropics). In contrast to Eq. (3), the kurtosis estimated from Eq. (4) can now have a positive excess kurtosis (depending on the value of p_0). However, the coefficient in front of S^2 predicted from Eq. (4) is still one, while the observed slope of a best linear fit between K and S^2 (Fig. 3) clearly shows that the coefficient should be larger than one.

a. The three-Gaussian model for temperature variability

We next extend our model to include also noise, which was done in Hughes et al. (2010) for the two-state Bernoulli

problem. Instead of constant T_c, $T_0 = 0$, and T_w, we take Gaussian distributions with mean values T_c, T_0, and T_w, and with standard deviation $\hat{\sigma}$ (see Fig. 4). This represents the random variability that can occur for the cold, near-zero, and warm temperature variations around their averages. The Gaussians around T_c and T_w represent the temperature anomalies associated with synoptic-scale features, while the Gaussian around T_0 represents small departures from the mean temperature. The width of the three Gaussians $\hat{\sigma}$ is chosen equal for simplicity, but in general the width can be different (and this assumption is probably a poor approximation in certain regions).

Taking the PDF to be

$$p = p_c N(-T_c, \hat{\sigma}) + p_0 N(0, \hat{\sigma}) + p_w N(T_w, \hat{\sigma}), \qquad (5)$$

where $p_w + p_c + p_0 = 1$ and $N(\mu, \hat{\sigma})$ represents a Gaussian distribution with mean μ and standard deviation $\hat{\sigma}$, we find (see section 4 in the supplemental material for further details)

$$\sigma^2 = \hat{\sigma}^2 + T_w T_c (1 - p_0) \qquad (6)$$

and

$$S = \frac{T_w T_c (1 - p_0)(T_w - T_c)}{\sigma^3}. \qquad (7)$$

We then further find that the kurtosis can be written as

$$K = aS^2 + b, \qquad (8)$$

where

$$a \equiv \frac{\hat{\sigma}^2}{T_w T_c (1 - p_0)} + 1 \qquad (9)$$

and

$$b \equiv \frac{1}{(1 - p_0)} \frac{1}{a^2} - \frac{3}{a^2} + 3. \qquad (10)$$

The coefficient $a = \hat{\sigma}^2/[T_w T_c(1 - p_0)] + 1$ essentially measures the ratio between the noise (given by width of Gaussians $\hat{\sigma}$) and the signal [related to the variance of the modified three-parameter Bernoulli system, $T_w T_c(1 - p_0)$]. The parameter b, for a given a, is then inversely related to $1 - p_0$. In section 4b we explore interesting limits of the three-Gaussian model, and in section 4c we demonstrate how different a and b parameters give rise to different decompositions of Gaussians, which ultimately control the non-Gaussian shape of the total PDF.

Note that the three-Gaussian PDF written in (5) was used in David et al. (2017) to examine the kurtosis and skewness structure of idealized barotropic ocean jets (see Fig. 9 in David et al. 2017), but the analytic expressions were not written explicitly or investigated further there.

b. Interesting limits of the three-Gaussian model

To explore proper limits of the expressions for a, b, S, and K achieved from the three-Gaussian model, we first define $\beta \equiv T_w T_c / \hat{\sigma}^2$. The parameter β is a dimensionless parameter
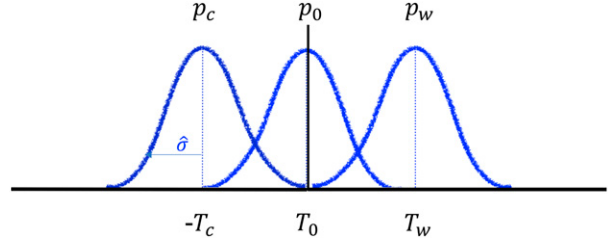

FIG. 4. A schematic illustrating the three-Gaussian model. In this model, the total PDF is written in terms of three Gaussians, describing the cold, near-zero, and warm anomalies. The mean values of these Gaussians are $-T_c$, $T_0 = 0$, and T_w; their amplitudes are p_c, p_0, and p_w, respectively; and their widths are denoted as $\hat{\sigma}$ (chosen equal for simplicity; see text). Note that the probabilities p_c, p_0, and p_w are are not necessarily equal, and satisfy by construction $p_c + p_0 + p_w = 1$.

describing the signal-to-noise ratio between the two-state Bernoulli system (with variance $T_w T_c$), and the noise given by the width of the Gaussians, $\hat{\sigma}$. For simplicity, we also denote $\gamma \equiv 1 - p_0$. Using these notations, the equations become

$$\sigma^2 = \hat{\sigma}^2(1 + \beta\gamma), \qquad (11)$$

$$S = \frac{\beta^{3/2}\gamma}{(1 + \beta\gamma)^{3/2}} S_0, \qquad (12)$$

and

$$K = \frac{\beta^2\gamma}{(1 + \beta\gamma)^2} S_0^2 + \frac{\beta^2\gamma(1 - 3\gamma)}{(1 + \beta\gamma)^2} + 3, \qquad (13)$$

where $S_0 = (T_w - T_c)/\sqrt{T_w T_c}$ is the skewness of the two-state Bernoulli distribution, and the parameters a and b are

$$a = \frac{1}{\beta\gamma} + 1 \qquad (14)$$

and

$$b = \frac{1}{\gamma a^2} - \frac{3}{a^2} + 3. \qquad (15)$$

Writing the equations in this form ensures we get the proper limits.

1) THE LIMIT $\beta \to 0$ (SMALL SIGNAL-TO-NOISE RATIO)

If the signal-to-noise ratio is small, $T_w T_c \ll \hat{\sigma}^2$ (i.e., the width of the PDFs is much larger than the two-state Bernoulli signal), then the means of the T_w and T_c Gaussians are effectively close to each other relative to their distance from the tails (since the width of the Gaussians is so wide). In this case, from Eqs. (11) to (15) $\hat{\sigma}^2 \to \sigma^2$, $S \to 0$, and $K \to 3$ (consistent with $a \to \infty$, $b \to 3$); that is, the PDF asymptotes to a normal distribution at the origin, and the concentrations at T_w and T_c become negligible.

2) THE LIMIT $\beta \to \infty$ (LARGE SIGNAL-TO-NOISE RATIO)

If the signal-to-noise ratio is large, $T_w T_c \gg \hat{\sigma}^2$ (i.e., the two-state Bernoulli signal is much larger than the width of the Gaussians), and then from Eqs. (11) to (15) one finds $\sigma^2 \to T_w T_c \gamma$, $S \to (1/\sqrt{\gamma}) S_0$,

and $K \to (1/\gamma)S_0^2 + 1/\gamma = S^2 + 1/\gamma$ (consistent with $a \to 1$, $b \to 1/\gamma$). These are exactly the results found earlier for the modified Bernoulli distribution with three variables [see Eq. (4)], that is, for the case of constant values of T_w, T_c, and T_0 with effectively zero noise.

3) THE LIMIT $\gamma \to 0$ ($p_0 \to 1$)

In the limit where the probability concentrates at the origin, around the T_0 Gaussian, the T_w and T_c Gaussians become negligible (recall that $p_w + p_c = 1 - p_0 = \gamma \to 0$). Equations (11)–(15) then give $\hat{\sigma}^2 \to \sigma^2$, $S \to 0$, and $K \to 3$ (and $a \to \infty$, $b \to 3$); that is, the PDF asymptotes again to a normal distribution at the origin, irrespective of the noise level.

4) THE LIMIT $\gamma \to 1$ ($p_0 \to 1$)

In the limit of $p_0 \to 0$, where the probability of the middle Gaussian becomes negligible, the problem reduces to the two-Gaussian problem studied in Hughes et al. (2010) (see section 5 in the online supplemental material for a derivation of the two-Gaussian case). Equations (11)–(15) now give $\sigma^2 \to \hat{\sigma}^2(1 + \beta)$, $S \to [\beta^{3/2}/(1 + \beta)^{3/2}]S_0$, and $K \to [\beta^2/(1 + \beta)^2]S_0^2 - [2\beta^2/(1 + \beta)^2] + 3$, corresponding to $a \to (1/\beta) + 1$ and $b \to -(2/a^2) + 3$.

These results essentially recover Hughes et al. (2010) (but a and b were not written explicitly there). Note that in their notation, $A = p_w$, $B = p_c$, $P = p_w p_c$, variance is set to one, and the width of the Gaussians is denoted σ (rather than $\hat{\sigma}$ as in our study). In addition, their solutions are written in term of d, which represents the distance (in units of standard deviations) between the two Gaussians, so $\hat{\sigma}d = T_w + T_c$ in our case. A comparison between the two- and three-Gaussian models is given in section 5c, where it is demonstrated that the added complexity in the three-Gaussian model is needed in order to successfully capture the correct temperature variability.

c. Interpreting the parameters a and b

Sattin et al. (2009) proposed that the parabolic relationship between kurtosis and skewness can be found in many physical systems obeying certain constraints. In the simplest case, assume that there is some parameter δ that controls the deviation from Gaussianity of the PDF. Hence, K and S are both functions of δ, and it is further assumed that $S(\delta)$ is smooth and invertible. This gives $\delta = \delta(S)$, and therefore $K = K(S)$. Expanding K in a Taylor series around small values of S (Sattin et al. 2009), one finds

$$K \simeq K_0 + \frac{S^2}{2}\frac{\partial^2 K}{\partial S^2}. \tag{16}$$

Here it was also assumed that the system is invariant with respect to the sign inversion, so the odd derivatives are zero since S is an odd function and K an even function with respect to the inversion operation. Note that the higher-order terms in this expansion can be neglected to a reasonable extent, given that the observed temperature skewness values are typically smaller than one (e.g., Fig. 2a).

From (16), it can therefore be identified that $b = K_0$ is the kurtosis that would exist in the absence of skewness. It is thus related to the relative frequency of the small (near-mean) and

the extremely strong (in the far tails) anomalies, compared to anomalies in the middle range, regardless of the sign. Setting $S = 0$ gives $K = b$, which implies that the sign of $b - 3$ determines whether the symmetric PDF would be platykurtic (negative excess kurtosis) or leptokurtic (positive excess kurtosis).

For the three-Gaussian model, we find that $b - 3 = 1/[(1 - p_0)a^2] - 3/a^2 = (1/a^2)[(3p_0 - 2)/(1 - p_0)]$. Hence, if $p_0 > 2/3$, the PDF with zero skewness has positive excess kurtosis, whereas if $p_0 < 2/3$ the PDF has a negative excess kurtosis. This is presented in Figs. 5a–d, which show examples of PDFs composed of the sum of three Gaussians, where the width of the total PDF is set to unity ($\sigma = 1$) and skewness to zero ($S = 0$ implying $T_w = T_c$), and we also arbitrarily set $a = 1.8$. This allows us to examine the effect of changing b, or effectively p_0, through $b = 1/[(1 - p_0)a^2] - 3/a^2 + 3$, on the PDF structure. For low values of b (and therefore p_0) (Figs. 5a–c), the PDF is indeed characterized by a negative kurtosis, indicated by the shallower-than-Gaussian peak and shorter-than-Gaussian tails, whereas for high values of b (and thus p_0) (Fig. 5d) the PDF is characterized by a positive kurtosis, indicated by the higher-than-Gaussian peak and longer-than-Gaussian tails. Note that the values of T_w, T_c, p_w, p_c, and $\hat{\sigma}$ in these idealized examples are determined from b (or p_0), a, σ, and S (see section 6 in the supplemental material).

As for the parameter a, from (16), it is clear that $a \equiv (1/2)(\partial^2 K/\partial^2 S)$. This also gives (for constant a) $a \equiv \partial K/\partial(S^2)$. Hence, a measures the sensitivity of K to changes in the "intensity" of skewness (i.e., to changes in skewness squared). The larger a is, the larger kurtosis K can be found for the same S^2. Moreover, for a given nonzero skewness S and a given b, a will determine if the PDF will have a positive or negative excess kurtosis. If $b > 3$ then $K = aS^2 + b$ will also be larger then 3, regardless of a (since $aS^2 > 0$). However, if $b < 3$, the PDF can still have a positive excess kurtosis if a is large enough.

In the three-Gaussian model $a = [\hat{\sigma}^2 + T_w T_c(1 - p_0)]/[T_w T_c(1 - p_0)] = \sigma^2/[T_w T_c(1 - p_0)]$, which can therefore be interpreted as the enhancement of the total variance of the three-Gaussian distribution, σ^2, compared to the variance of the modified Bernoulli distribution with three variables, $T_w T_c(1 - p_0)$. Alternatively, $a = \hat{\sigma}^2/[T_w T_c(1 - p_0)] + 1$ can be interpreted as the ratio (plus 1) between the noise in the system, given by the width $\hat{\sigma}^2$ of the Gaussians, to the signal, defined here as the modified Bernoulli distribution with three variables. Hence, the signal-to-noise ratio is related to how well separated the Gaussians are compared to their width.

From its definition, it is clear that $a \geq 1$ (with $a = 1$ only achieved for the modified Bernoulli system with three parameters, where $\hat{\sigma} = 0$). Figures 5e–h show PDFs composed of the sum of three Gaussians with varying a, where the total width of the PDF is again set to unity ($\sigma = 1$), and we also set skewness to $S = 0.4$ and $b = 2.7$ (hence b in the case of zero skewness would give a negative excess kurtosis). For low values of a (Fig. 5e) we find narrow PDFs that are more distant from each other, and the PDF becomes trimodal (which is not what is usually found for realistic low-level temperature distributions). In this case, the excess kurtosis is negative ($K < 3$) because the localization of the signals effectively make the Gaussian longer in the tails. As a increases (Figs. 5e–g), the PDFs become wider and closer to each other (the signal-to-noise ratio decreases) until eventually a
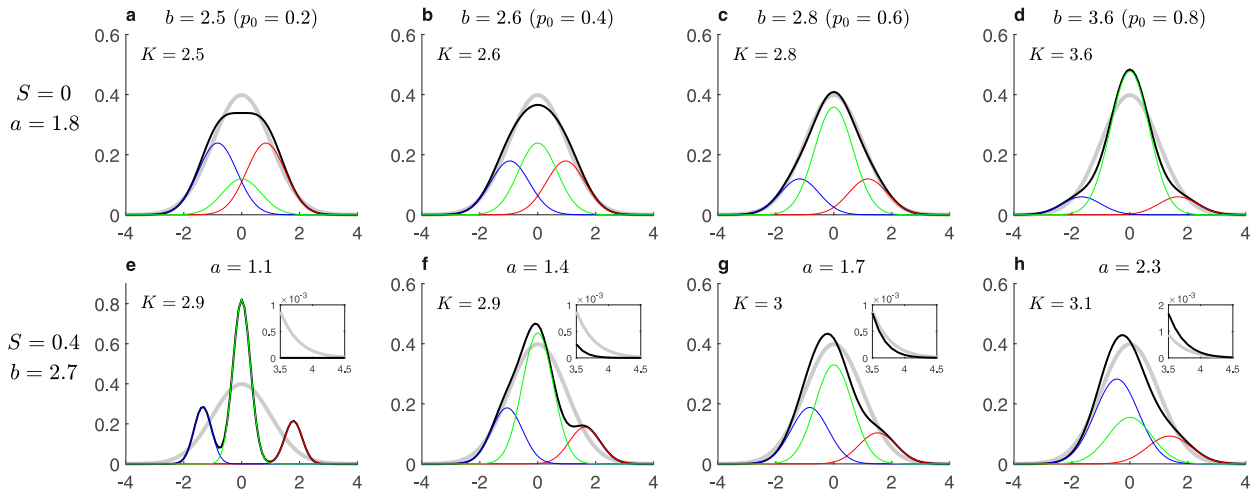
FIG. 5. Idealized examples of PDFs composed of the sum of three Gaussians, with varying a and b, to explore their influence on the shape of the total PDF. (a)–(d) a is held constant at a fixed value of $a = 1.8$, and skewness is set to zero ($S = 0$ implying $T_w = T_c$). The values of b—or effectively p_0, through $b = 1/[(1 - p_0)a^2] - 3/a^2 + 3$—are (a) $b = 2.5$ (corresponding to $p_0 = 0.2$), (b) $b = 2.6$ (corresponding to $p_0 = 0.4$), (c) $b = 2.8$ (corresponding to $p_0 = 0.6$), and (d) $b = 3.6$ (corresponding to $p_0 = 0.8$). (e)–(h) b is held constant at a fixed value of $b = 2.7$, and skewness is set to $S = 0.4$. The values of a, which effectively control the signal-to-noise-ratio, are (e) $a = 1.1$, (f) $a = 1.4$, (g) $a = 1.7$, and (h) $a = 2.3$. In all cases, the width of the total PDF is set to unity ($\sigma = 1$), and a Gaussian distribution with a unit width is shown for reference with a gray line. The resulting kurtosis is given in the upper-left corner of each panel. In (e)–(h), the upper-right box is a zoom-in into the right positively skewed tail.

is large enough (Fig. 5h) such that the overall PDF has a positive excess kurtosis ($K > 3$) and the right-skewed tail becomes longer than a Gaussian (see boxes in Figs. 5e–h, which show a zoom into the region of the right-skewed tail).

Hence, different a and b values can give very different PDF structures, from trimodal distributions to unimodal PDFs with a non-Gaussian shape. In the following sections, we estimate the parameters a and b from the linear relationship between K and S^2, first in a longitudinally independent form and then for different local regions, and explore the resulting PDF decompositions, their interpretation, and their projected changes.

5. The latitudinal dependence of $\tilde{K} = aS^2 + b$

For clarity, we henceforth denote the actual kurtosis as K, while the approximated kurtosis is denoted as $\tilde{K} = aS^2 + b$. The coefficients a, b of the approximated kurtosis can be estimated for each latitude by taking all longitudinal points and finding a best linear fit between K and S^2. The resulting dependence on latitude is shown in Fig. 6 (after applying a customary smoothing with respect to latitude using MATLAB's "smooth" function). Also shown for completeness are the zonally averaged skewness $S(y)$ (Fig. 6a) and the zonally averaged excess kurtosis $K(y) - 3$ (Fig. 6b). Note however that the zonal averages hide a lot of the regional structure in the NH. For example, the skewness is generally very small in the zonal mean, but Fig. 2a shows that this is a result of compensation between strong positive skewness in northern oceans and strong negative skewness, particularly over the west coast of North America. Nonetheless, the purpose here is to get the general latitudinal dependence of the parameters a and b, even if they might vary longitudinally. Moreover, since we are not

averaging, but rather taking all longitudinal points in a given latitude, even if K and S vary significantly longitudinally they might still possess the same relationship in terms of the fit $K = aS^2 + b$.

The coefficient $a(y)$ is generally high in the tropics and lower in the midlatitudes (Fig. 6c). Note that the 850-hPa level intersects topography, and we have thus limited our analysis here to 75°S–75°N. The parameter $b(y)$ is also high in the tropics and achieves the lowest value in the middle of the SH jet (where skewness is zero) (Fig. 6d). The frequency p_0 of the near-zero anomalies [calculated by plugging a and b in relation (10) and inverting it to find p_0] is generally similar to b (Fig. 6e). The overall recovered excess kurtosis, $\tilde{K} - 3 = aS^2 + b - 3$ (Fig. 6f), is indeed similar to the zonally averaged kurtosis (Fig. 6b) and captures its main features.

The estimated coefficients $a(y)$ and $b(y)$ can also be used to plot a spatial map of the estimated excess kurtosis $\tilde{K} - 3 = a(y)S^2 + b(y)$ (i.e., the same coefficients a and b are used for every longitude as a function of latitude only, but we keep the full spatial field of skewness; Fig. 2c). This recovers well the excess kurtosis structure (a spatial correlation coefficient of 0.85), albeit with somewhat lower values (see Fig. S2). For example, it captures the high kurtosis values in the tropics (which are not achieved for the simplified relation $K = S^2 + 1$; see Fig. S1), and also the high kurtosis values on the poleward flanks of the midlatitude storm track regions and on the west coast of North America.

a. The relation between K and S in the SH midlatitudes

The relation between K and S is demonstrated for the SH midlatitudes. The skewness dipole around the SH midlatitude jet can be clearly seen in Fig. 6a. In the middle of the SH jet
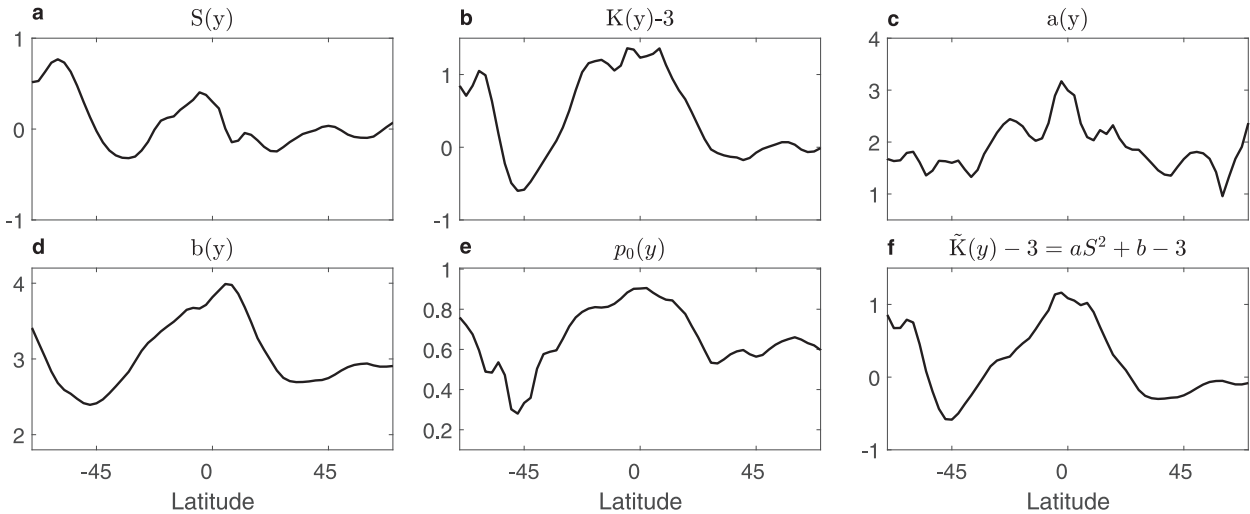
FIG. 6. The latitudinal distribution of the 850-hPa (a) zonally averaged skewness $S(y)$, (b) zonally averaged excess kurtosis, the estimated parameters (c) $a(y)$, (d) $b(y)$, and (e) $p_0(y)$, and (f) the recovered excess kurtosis $\tilde{K}(y) - 3 = a(y)S^2(y) + b(y) - 3$, based on ERA-Interim data averaged for the period 1980–2015 during DJF. The parameters $a(y)$ and $b(y)$ are estimated by calculating, for each latitude separately, the coefficients a, b of $\tilde{K} = aS^2 + b$, by fitting a linear relation between K and S^2 in all the corresponding longitudinal points. The parameter $p_0(y)$ is then estimated from $a(y)$ and $b(y)$ using the relation $b(y) = \{1/[1 - p_0(y)]\}[1/a(y)^2] - 3/a(y)^2 + 3$.

axis, around 45°S, skewness is zero and kurtosis achieves its minimum. From (8), it is clear that $\tilde{K} \approx b$ since $S \approx 0$. The minimum of b (Fig. 6d) is consistent with a minimum in p_0 (Fig. 6e), since $b = [1/(1 - p_0)]1/a^2 - 3/a^2 + 3$, and a is roughly constant in the SH midlatitudes.

The interpretation of these findings is as follows. The center of the jet roughly describes a jump between cold polar air and warmer subtropical air. As the jet meanders, the region beneath it will always be in either a cold anomaly state or a warm anomaly state. Close to the jet center, the system will spend a similar fraction of time in either one of these states (cold or warm), and the magnitude of cold and warm anomalies is similar since the meridional background temperature gradient is roughly symmetric around the jet axis. Hence, in this region, we can expect $S \approx 0$, and also $p_w \approx p_c \approx p_0 \approx 1/3$ [as is indeed found in Fig. 6e, with min(p_0) $\approx 1/3$]. Thus, kurtosis is smallest at the center of the jet both because S is smallest (zero), and because p_0 achieves a minimum there.

Away from the jet center, the system spends more time around its average temperature (p_0 increases; Fig. 6e) and an asymmetric fraction of time in the cold/warm states. Nonlinear meridional advection results in an equatorward (poleward) movement of cold (warm) anomalies, and hence stronger magnitudes of cold (warm) anomalies on the equatorward (poleward) side of the jet. Correspondingly, a negative (positive) skewness is generated on the equatorward (poleward) side of the jet. Consistent with this, kurtosis (which is proportional to S^2) increases away from the jet axis (Fig. 6b). A similar interpretation was given in Hughes et al. (2010) and in David et al. (2017) for ocean jets.

b. The three-Gaussian interpretation for the SH midlatitudes

More intuitively, these results can be directly seen by inspecting the three-Gaussian model decomposition (Fig. 7).

The seven unknowns in the model ($\hat{\sigma}$, T_c, T_0, T_w, p_c, p_0, and p_w) can be found as follows. First, from the normalization of the PDF, we have $p_0 = 1 - p_w - p_c$. Next, we set $T_0 = 0$, and from the first-order moment of the PDF (the mean) we thus also have $T_w p_w = T_c p_c$. The second- and third-order moments [given in (6) and (7), respectively] give two more equations for the known variance and skewness. Last, from the fit between K and S^2 we have two more equations for the estimated coefficients a and b [given in (9) and (10), respectively]. Hence, inverting these relations (see section 6 in the supplemental material for full derivation), we can find all the model parameters. Note that kurtosis is thus not used directly. Rather, we are using the fitted relationship between K and S^2 to extract more information about the system.

The three-Gaussian decomposition is illustrated for three latitudinal regions in the SH midlatitudes (30°–40°, 45°, and 55°–75°S). The actual PDFs (referred to as "raw" but presented with a kernel density smoother) are shown in black in the first row of Fig. 7. For comparison, their corresponding Gaussian distributions (i.e., same variance but with $S = 0$, $K = 3$) are shown in red. Equatorward of the SH jet (30°–40°S; Fig. 7a), the positive warm tail is shorter than a Gaussian, while the negative cold tail is longer than a Gaussian, consistent with the negative skewness there ($S = -0.2$). In addition, kurtosis is larger than that of a Gaussian ($K = 3.3$). The three-Gaussian model decomposition (Fig. 7c) gives $T_w \approx 3.3$ and $T_c \approx 4.9$. Hence, equatorward of the jet, the mean intensity of cold anomalies is larger than that of warm anomalies ($T_c > T_w$) (recall that anomalies are measured relative to the background field, which is warm in this region). Consistent with this, the decomposition also shows that averaged cold anomalies occur less frequently, $p_c < p_w$ ($p_w \approx 0.25$ and $p_c \approx 0.17$). This is a simple consequence of the zero mean of the entire distribution ($p_w T_w - p_c T_c = 0$); that is, the stronger anomalies must be less frequent in order for
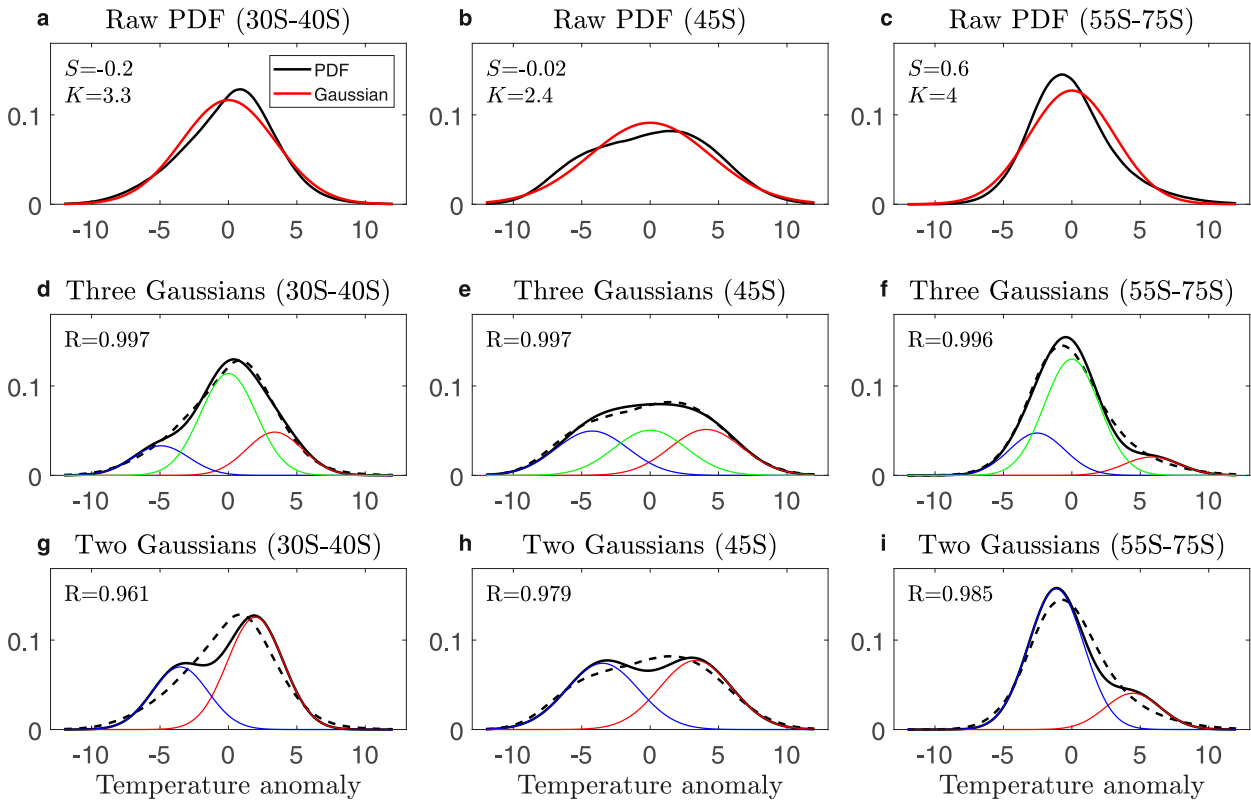
FIG. 7. Examples of the three-Gaussian vs the two-Gaussian decomposition for the SH midlatitudes. (a)–(c) The 850-hPa raw temperature PDFs (black line) for anomalies at the latitudinal bands (a) 30°–40°S, (b) 45°S, and (c) 55°–75°S, based on ERA-Interim data averaged over the years 1980–2015 during DJF. The red lines show the corresponding Gaussian distributions (the same variance but setting skewness to 0 and kurtosis to 3). (d)–(f) The approximated PDFs based on the three-Gaussian model for the same latitudinal bands, respectively. The thin blue and red lines are the Gaussians representing the cold and warm anomalies, respectively, while the green Gaussian represents the near-zero anomalies. The sum of the three Gaussians is shown by the thick black line, which recovers well the shape of the corresponding raw PDF, shown in dashed black for reference. (g)–(i) The corresponding decomposition but for the two-Gaussian model, calculated in the same manner but assuming $p_0 = 0$. The correlation coefficients for the match between the model and the raw PDFs for each case is denoted in the upper-left corner of each panel. The parameters used for finding the three Gaussians are derived from the variance, skewness, kurtosis, a, and b, calculated for each region of interest separately (see section 6 in the supplemental material for more details).

the total time-mean anomaly to be zero. However, note that the very extreme cold anomalies (left tail in the Gaussian describing T_c; blue line in Fig. 7c) have a higher probability than very extreme warm anomalies (right tail in the Gaussian describing T_w, red line in Fig. 7c). Hence, while the averaged cold anomalies occur less frequently (to conserve zero time-mean anomaly in total), extremely strong cold anomalies have a higher probability than extremely strong warm anomalies. These results are exactly the characteristics of the negative skewness found in this region. The three-Gaussian model also reveals that the frequency p_0 ($p_0 \approx 0.58$; that is, the frequency of small departures from the mean) is significantly higher than either p_w or p_c. The high p_0 together with the nonzero skewness are what give rise to the positive excess kurtosis found in this region.

In the center of the SH jet (45°S; Fig. 7b), skewness is almost zero ($S \approx -0.02$) and kurtosis is low ($K \approx 2.4$). The three-Gaussian decomposition now gives (Fig. 7e) $T_w \approx 4$ and $T_c \approx 4.2$ (hence $T_w \approx T_c$) and $p_w \approx p_c \approx p_0 \approx 1/3$. Hence, T_w and T_c

anomalies occur at similar magnitudes, and at similar frequencies as T_0. This confirms our previous interpretation of the underlying dynamics at the center of the jet, discussed in section 5a.

Poleward of the jet (55°–75°S; Fig. 7c), we find the opposite result compared to the equatorward side. In this region the model predicts stronger warm anomalies, $T_w > T_c$ ($T_w \approx 5.8$ and $T_c \approx 2.5$), which occur on average less frequently, $p_w < p_c$ ($p_w \approx 0.1$ and $p_c \approx 0.24$), but with a much longer warm tail overall. In addition, we find higher frequency of near-zero anomalies ($p_0 \approx 0.66$). These results are consistent with the high positive skewness ($S \approx 0.6$) and higher than Gaussian kurtosis ($K \approx 4$) found in this region.

In each case shown in Figs. 7d–f, the overall sum of the three Gaussians (black line) recovers well the actual PDF in the region (shown in black in Figs. 7a–c and given by the dashed black line in Figs. 7d–f for ease of comparison). The corresponding correlation coefficient is reported in the upper left corner of each panel.

Fig(s). 7 live 4/C

To summarize, the model allows us to truncate the full PDF (which has an infinite number of moments) into a sum of three Gaussians. These illustrate directly the main ingredients of the underlying PDF, namely the mean intensity of cold, near-zero, and warm anomalies, their frequencies, and width. These recover the variance, skewness, and the parabolic relation between kurtosis and skewness by construction, but also give a much simpler interpretation of the temperature variability characteristic of the region.

c. Comparing the two- versus three-Gaussian model

The two-Gaussian model developed in Hughes et al. (2010) also predicts a squared relation between kurtosis and skewness, and has fewer free parameters than the three-Gaussian model (since $p_0 = 0$). However, the latter gives a much better match to the observed temperature variability. Specifically, the two-Gaussian model predicts the relation $b = -2/a^2 + 3$, which is not what we find from the data (Fig. S3). Similarly, the predicted excess kurtosis from the two-Gaussian model, namely $K = a(y)S^2 - 2/a(y)^2 + 3$, does a poor job of recovering the actual excess kurtosis, with too negative values almost everywhere (Fig. S4). No similar comparison can be made with the three-Gaussian model because we are using the estimated kurtosis (or, more directly, a and b) to estimate the parameters of the three Gaussians (i.e., we have another free parameter p_0 that is unknown, and this parameter is estimated using a and b).

For further comparison, we repeat the PDF decomposition analysis shown in Figs. 7d–f for the same SH latitudinal bands, but for the two-Gaussian model. As can be seen, while the fit is still good for the two-Gaussian model, the match is clearly reduced. In all cases, the three-Gaussian model provides a better match to the full PDF compared to both a Gaussian distribution and the two-Gaussian model. Specifically, the latter clearly underrepresents anomalies around the mean, which can result in a bimodal PDF (which is not usually found for low-level temperature). Hence, the three-Gaussian model gives a better fit even if the raw PDF is a unimodal distribution, allowing us to correctly capture its non-Gaussian shape.

The discussions above for the latitudinal dependence of the relation $\tilde{K} = aS^2 + b$ are focused on the SH midlatitudes during DJF (which are primarily over ocean regions) since the parameters a and b are estimated for all longitudinal points in a given latitude, and these estimates are probably more accurate over nearly zonally homogeneous regions (such as the SH midlatitudes). Indeed, different parabolic relationships between skewness and kurtosis (i.e., different a and b parameters) are found for land versus ocean regions in the NH with the same latitudinal positions and the same zonal extent (see Fig. S5). These differences are not captured in Fig. 6, which takes all longitudinal points in a given latitude together and fits one value for $a(y)$ and one for $b(y)$. The motivation for estimating $a(y)$ and $b(y)$ is to produce a spatial map of the estimated excess kurtosis using S^2. Ideally, a and b should be evaluated at the grid point level, but since this is not possible we fit it to the longitudinally independent coefficients. However, the fact that $K - 3$ (Fig. 2b) is recovered relatively well by $\tilde{K} - 3 = a(y)S^2 + b(y) - 3$ (Fig. 2c; see also

Fig. S2) implies that this is not such a bad approximation, and that in fact most of the zonal structure in kurtosis is originating from the structure of S^2. Nonetheless, in section 6b we estimate a and b locally for different regions over the globe, and investigate their three-Gaussian decompositions and projected changes.

6. Interpreting future temperature variability changes

We next investigate the projected higher-order temperature variability changes using an ensemble of 26 CMIP5 models driven by the RCP8.5 emissions scenario. Specifically, we concentrate on the skewness and kurtosis changes (Fig. 8). The first row shows the historical values (Figs. 8a,b), which are very similar to the results found for the ERAI data (Figs. 2a,b), and the second row shows the corresponding projected changes of skewness (Fig. 8c) and kurtosis (Fig. 8d).

The model developed here can be used to better understand the future temperature variability changes in two different ways. First, from the approximate expression for kurtosis $\tilde{K} = aS^2 + b$, we can inspect how each of the changes in a, b, and S^2 influence changes in $\tilde{K}$. Second, using the three-Gaussian PDF given in (5), we can examine how each one of the changes in p_c, p_0, p_w, T_c, T_w, and $\hat{\sigma}$ contributes to the overall change in the temperature PDF. This enables easier visualization and understanding of the projected temperature changes in different regions over the globe.

a. Decomposition of kurtosis changes

From the relation $\tilde{K} = aS^2 + b$, we can decompose the projected kurtosis changes in terms of changes in a, b, and S^2 as

$$\Delta\tilde{K} = S^2\Delta a + a\Delta(S^2) + \Delta b. \qquad (17)$$

Each of the terms in (17) can be estimated separately from the historical and projected simulations. For simplicity, we consider here only the longitudinally independent estimations $a(y)$ and $b(y)$, but keep the full spatial field of skewness. The actual projected excess kurtosis change (shown again in Fig. 9a for ease of comparison) is captured well by the estimated projected excess kurtosis change $\Delta(\tilde{K} - 3) = \Delta\tilde{K} = \Delta(aS^2 + b)$ (Fig. 9b), with a relatively small difference (and a spatial correlation coefficient of 0.76), showing the largest discrepancies in the tropics.

The advantage of examining the estimated kurtosis change is that we can now decompose it into each of the terms in (17) for $\Delta\tilde{K}$. The decomposition in Figs. 9d–f shows that the estimated kurtosis change is dominated by the skewness squared changes, through the term $a\Delta(S^2)$ (Fig. 9e), while the other terms are considerably smaller (Figs. 9d,f). Even though these are calculated for $a(y)$ and $b(y)$ only, it is clear from comparing Figs. 9a and 9b that these are reasonable approximations, and that indeed most of the change in kurtosis originates from the changes in the skewness squared. This implies that kurtosis changes can be predicted to first order by the skewness squared changes:

$$\Delta\tilde{K} \approx a\Delta(S^2) = 2aS\Delta S. \qquad (18)$$

It is easy to see from (18) that if skewness changes oppose the historical skewness $[S\Delta(S) < 0]$, then the kurtosis change
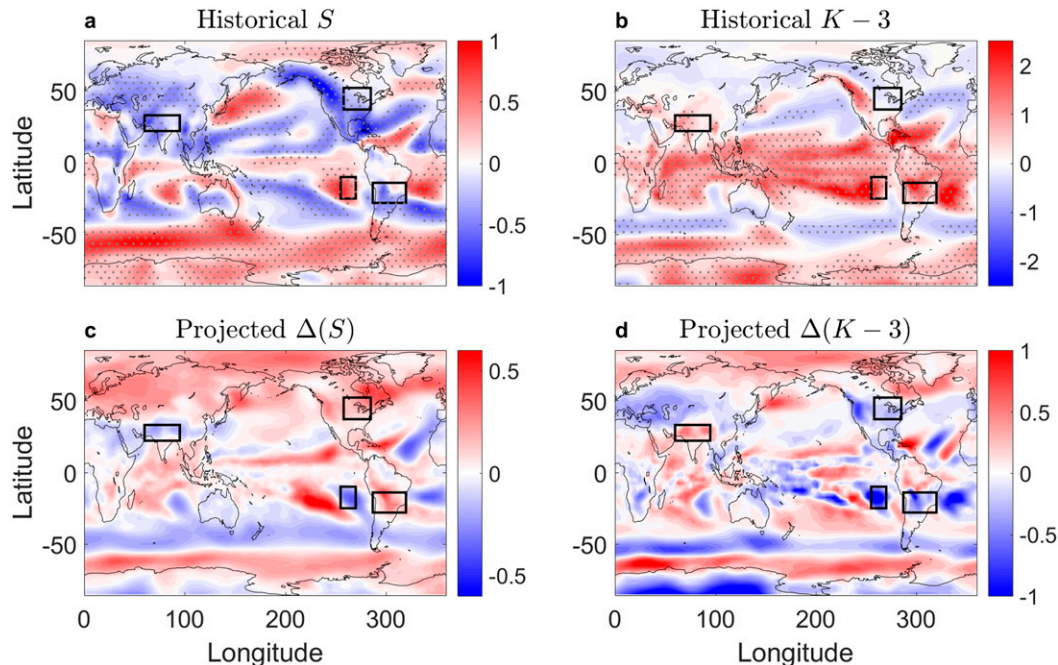
FIG. 8. The historical (1981–99) ensemble-mean temperature skewness and kurtosis, and their projected changes (2081–99 minus historical), based on 26 CMIP5 RCP8.5 ensemble members. The 850-hPa temperature (a) skewness and (b) kurtosis during DJF, and (c),(d) the corresponding projected changes. Regions where the skewness and kurtosis values are statistically significant are stippled. The black boxes highlight regions of interest that are further explored in Fig. 10.

will be negative, while if the skewness change reinforces the historical skewness $[S\Delta(S) > 0]$ then the kurtosis change will be positive. In other words, if the change in the asymmetry between cold and warm anomalies increases, then kurtosis increases too, since more of the PDF must lie in one of the tails (and vice versa if the asymmetry decreases).

In addition, (18) implies that the meridional advection arguments used in previous studies (Garfinkel and Harnik 2017; Linz et al. 2018; Tamarin-Brodsky et al. 2019; Linz et al. 2020; Tamarin-Brodsky et al. 2020) to explain skewness changes can also be used to understand kurtosis changes. For example, it was suggested that the skewness increase projected over most of the NH during winter (Fig. 8c) can be understood by linear advection arguments (Tamarin-Brodsky et al. 2020), since cold anomalies advected from the Arctic encounter a significantly reduced background temperature gradient compared to warm anomalies advected from the tropics (and the cold anomalies therefore weaken more than the warm anomalies). The positive skewness change, together with the spatial structure of the historical skewness (Fig. 8a), are enough to understand the sign of the projected kurtosis changes (Fig. 8d); these are generally positive where the sign of ΔS is the same as S, and negative where the sign of ΔS is opposite to that S, as predicted from (18).

We note however that in some regions, the contributions from changes in a, and especially b, could be important too (as seen from Figs. 9d,f) and could reflect changes in extremes that

do not contribute directly to an asymmetry between cold and warm anomalies (e.g., through changes in $\hat{\sigma}$ or p_0).

b. The three-Gaussian paradigm for interpreting future temperature changes

The three-Gaussian paradigm can also be useful for interpreting regional temperature variability and its projected changes. To show this, we examine several regions over the globe, chosen because they represent very distinct temperature responses. The coefficients a and b in $\tilde{K} = aS^2 + b$ can be estimated as before, but now locally for each region of interest. This is done by aggregating S and K over the specific grid points defining the region and over all the 26 CMIP5 models, and finding the best linear fit between K and S^2. From these regional parameters of a and b and from the regionally averaged values of the mean, variance, and skewness, we then find, separately for the historical and projected simulations, the parameters describing the three-Gaussian model (as was done before from the SH midlatitudes; see section 6 in the supplemental material), namely T_w, T_c, p_w, p_c, p_0, and $\hat{\sigma}$ (recall that by construction $T_0 = 0$). This allows us to translate the problem from changes in the higher-order temperature moments such as skewness and kurtosis, which are generally harder to interpret, to changes in the amplitude and frequency of cold, warm, and averaged anomalies. The three-Gaussian paradigm also allows for a simple visualization of the decomposition of the underlying PDF and its projected changes.
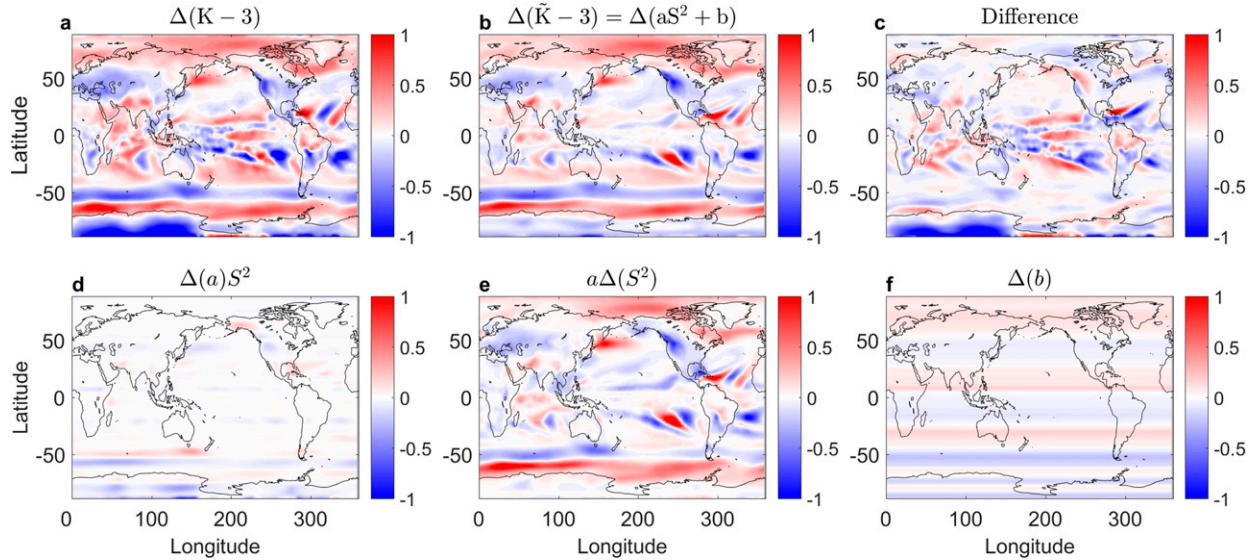
Fig(s). 8 live 4/C

FIG. 9. Projected kurtosis change and its decomposition, based on 26 CMIP5 RCP8.5 ensemble members at the 850-hPa level during DJF. The (a) projected excess kurtosis change $\Delta(K-3)$, (b) total change in the estimated excess kurtosis $\Delta(\tilde{K}-3) = \Delta(aS^2+b)$, and (c) their difference, and the decomposition of the approximated kurtosis change into (d) $\Delta(a)S^2$, (e) $a\Delta(S^2)$, and (f) $\Delta(b)$. Here the longitudinally independent estimations $a(y)$ and $b(y)$ are used, while for skewness the full $S(x,y)$ field is used.

As an example, we consider the following regions, highlighted by the black boxes in Fig. 8: central-east North America (37°–52°N, 258°–285°E), the eastern tropical Pacific cold tongue (10°–25°S, 255°–270°E), the northern part of South Asia (22°–33°N, 60°–95°E), and middle South America (14°–28°S, 287°–320°E). These regions have different signs of skewness and kurtosis, and also experience different combinations of projected skewness and kurtosis changes. For example, central-east North America is characterized by negative skewness and excess kurtosis and experiences a positive skewness and a negative excess kurtosis change (Figs. 8 and 10a). The eastern tropical Pacific cold tongue is characterized by positive skewness and excess kurtosis and experiences a negative skewness and excess kurtosis change (Figs. 8 and 10b). The northern part of South Asia is characterized by negative skewness but a slightly positive excess kurtosis and experiences a negative skewness and a positive excess kurtosis change (Figs. 8 and 10c). And finally, middle South America is characterized by negative skewness and a positive excess kurtosis and experiences a positive skewness and a negative excess kurtosis change (Figs. 8 and 10d). Thus, these regions depict very different temperature variability signatures and distinct responses to climate change.

We now show how the three-Gaussian decomposition can aid the interpretation of the temperature PDF and its projected changes. For central-east North America (Fig. 10e) in the historical simulations, we find $T_c = 9.4$, $T_w = 7$, $p_c = 0.19$, $p_w = 0.25$, and $p_0 = 0.56$. Thus, the averaged magnitude of cold anomalies T_c is larger than T_w in this region, but they occur less frequently (i.e., $p_c < p_w$, consistent with the constraint $p_w T_w = p_c T_c$). However, as opposed to averaged cold anomalies, the extreme cold anomalies (in the extreme left tail of the PDF describing the historical cold anomalies; blue solid line in Fig. 10e) have a higher probability of occurrence compared to extreme warm

anomalies (in the extreme right tail of the PDF describing the historical warm anomalies; red solid line in Fig. 10e). These characteristics are exactly consistent with the negative skewness found in this region in the historical simulations. In the projected climate, the cold and warm Gaussians become of similar magnitude and frequency, as cold anomalies weaken significantly and become more frequent ($T_c = 6.7$, $T_w = 6.7$, $p_c = 0.25$, and $p_w = 0.25$). The decrease of extreme cold anomalies and the increase in frequency of average cold anomalies is also accompanied by a slight decrease in the frequency of the T_0 Gaussian (from $p_0 = 0.56$ in the historical simulations to $p_0 = 0.51$ in the projected simulations) and a decrease in the width of the Gaussians (from $\hat{\sigma} = 4.6$ to $\hat{\sigma} = 4.2$). These changes are consistent with the positive skewness change $\Delta S = 0.19$ (as the asymmetry between cold and warm anomalies decreases), negative kurtosis change $\Delta K = -0.12$ (less frequency of extreme events), and the variance or standard deviation decrease $\Delta \sigma = -0.71$ (as both cold and warm anomalies weaken).

Similarly, the PDF decomposition in the eastern tropical Pacific cold tongue (Fig. 10f) shows how warm anomalies are stronger but less frequent on average ($T_c = 1.4$ and $T_w = 3.2$ with $p_c = 0.2$, $p_w = 0.1$), while extreme warm anomalies are more frequent than extreme cold anomalies, consistent with the positive skewness there. In the projected climate, there is a negative skewness change ($\Delta S = -0.18$) as mean cold anomalies slightly intensify while warm anomalies slightly weaken ($T_c = 1.6$, $T_w = 3$, $p_c = 0.25$, $p_w = 0.5$), so the asymmetry decreases. In addition, the frequency of the T_0 Gaussian decreases in the future climate (from $p_0 = 0.7$ to $p_0 = 0.6$), and the width of the Gaussians slightly increases (from $\hat{\sigma} = 1$ to $\hat{\sigma} = 1.2$), consistent with the negative kurtosis change ($\Delta K = -0.64$) and positive variance increase ($\Delta \sigma = 0.29$) there. Note that even though more of the PDF lies at the
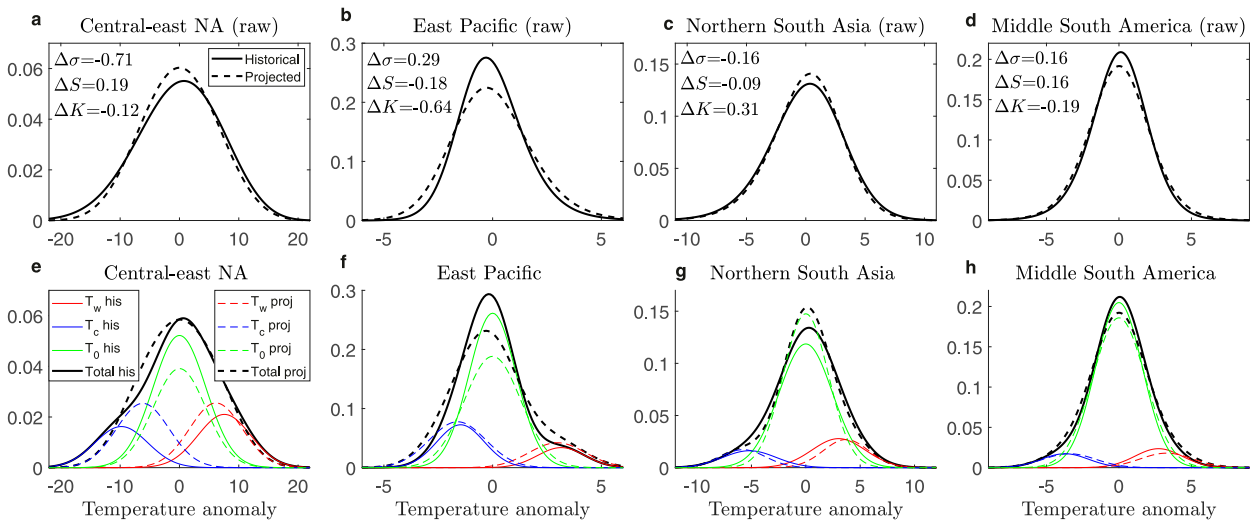
Fig(s). 9 live 4/C

FIG. 10. Examples of the three-Gaussian decomposition of temperature PDF and its projected changes for different regions over the globe. (a)–(d) The historical (solid) and projected (dashed) raw temperature PDF at (a) central-east North America, (b) the eastern tropical Pacific cold tongue, (c) the northern part of South Asia, and (d) middle South America, based on 26 CMIP5 RCP8.5 ensemble members at the 850-hPa level during DJF. The associated region-averaged standard deviation, skewness, and kurtosis changes are denoted $\Delta\sigma$, ΔS, and ΔK, respectively, and shown in the upper-left corner of each panel. (e)–(h) The approximated PDFs based on the three-Gaussian model for the same regions, respectively. The thin solid (dashed) blue, green, and red lines are the historical (projected) Gaussians representing the cold, near-zero, and warm anomalies, respectively. The sum of the three Gaussians for the historical (projected) simulations is shown by the black solid (dashed) line in each panel, which roughly recovers the shape of the corresponding raw PDF. The parameters used for finding the three Gaussians are derived from the mean, variance, skewness, a, and b, calculated for each region of interest separately (see section 6 in the online supplemental material for more details).

extreme end in the projected climate, the kurtosis change is overall negative due to the strong decrease in p_0.

In the northern part of South Asia (Fig. 10g), there is a negative skewness in the historical simulations ($T_c = 5.2$, $T_w = 3.0$, and $p_c = 0.09$, $p_w = 0.17$). In the projected climate, the means of both cold and warm anomalies intensify (but cold anomalies slightly more) and become less frequent ($T_c = 5.8$, $T_w = 3.8$, and $p_c = 0.09$, $p_w = 0.13$), consistent with the negative skewness change ($\Delta S = -0.09$). In addition, the frequency of the T_0 Gaussian increases in the future climate (from $p_0 = 0.72$ to $p_0 = 0.77$) and the width of the Gaussians decreases (from $\hat{\sigma} = 2.4$ to $\hat{\sigma} = 2.0$), consistent with the positive kurtosis change ($\Delta K = 0.31$) and negative variance change ($\Delta\sigma = -0.16$). Even though the mean intensities of both cold and warm anomalies intensify, not much overall change is found in the extremes of the PDF since the width of the Gaussians decreases.

Finally, in middle South America (Fig. 10h), the negative skewness ($T_c = 3.7$, $T_w = 2.7$, $p_c = 0.06$, $p_w = 0.09$) becomes less negative ($\Delta S = 0.16$) as mean cold anomalies slightly weaken and mean warm anomalies intensify ($T_c = 3.5$, $T_w = 3.3$, $p_c = 0.07$, $p_w = 0.07$), so the asymmetry decreases. In addition, the frequency of the T_0 Gaussian slightly decreases (from $p_0 = 0.84$ to $p_0 = 0.8$), and the width of the Gaussians slightly increases (from $\hat{\sigma} = 1.6$ to $\hat{\sigma} = 1.78$), consistent with the negative kurtosis change ($\Delta K = -0.19$) and the small variance increase ($\Delta\sigma = 0.16$) found in this region.

The advantage of the three-Gaussian paradigm is that it allows for a clear visualization of the PDF and its projected changes in terms of the changes in the cold, near-zero, and warm anomalies, separately. Such changes in the frequency and magnitude of cold

and warm anomalies are generally easier to interpret and communicate than changes in skewness and kurtosis.

7. Summary and discussion

In this work, a simple model based on Hughes et al. (2010) and David et al. (2017) is used to capture the essence of atmospheric temperature variability and its projected changes, including the higher-order moments (which are often ignored). In this model, the temperature PDF is represented by three Gaussians, representing the cold, near-zero, and warm anomalies. The cold and warm Gaussians represent the larger temperature fluctuations associated with synoptic-scale weather systems, while the near-zero Gaussian represents small deviations from the mean temperature. The three-Gaussian model captures the observed relationship between kurtosis and skewness squared. Moreover, the coefficients of the relation $\tilde{K} = aS^2 + b$ can be estimated directly from data. From a, b, and the first three moments describing the temperature PDF, the parameters describing the three Gaussians can be found. This allows for a simpler visualization and interpretation of the PDF in different regions.

A number of models with increasing complexity were presented. First was the simple two-state Bernoulli distribution, which assumes that anomalies can have a fixed amplitude of either T_w or T_c. The Bernoulli distribution is helpful for capturing the observed skewness structure (Tamarin-Brodsky et al. 2020) but fails to correctly capture the temperature kurtosis. Physically, this is because none of the distribution is assumed to lie around the mean, and also because the localization of the signal around T_c, T_w

makes the tails short compared to a Gaussian (hence it always gives negative excess kurtosis). Nonetheless, its simplicity [Eqs. (2) and (3)] is helpful and can be useful for studying temperature skewness and variance in different applications (e.g., Tamarin-Brodsky et al. 2020). A slightly more complex model (referred to here as the modified three-parameter Bernoulli distribution) also includes the mean value T_0, which gives more realistic excess kurtosis values because it now also accounts for the weight of the distribution around the mean. Finally, the modified three-parameter Bernoulli distribution was extended to include noise by allowing the T_c, T_0, and T_w anomalies to fluctuate around their means. This is a much more physically realistic model, referred to here as the three-Gaussian model, which recovers by construction not just the first three moments of the temperature PDF, but also the observed relationship between kurtosis and skewness squared (and thus also recovers the approximated kurtosis by construction). The Gaussians allow the tails of the distributions to be captured as well, and thus kurtosis can also be accounted for. While the simpler two-Gaussian model of Hughes et al. (2010) also predicts a squared relationship between kurtosis and skewness, it is shown here that it underrepresents kurtosis (and therefore does not match the actual PDFs as well) since it does not account for the weight of the distribution around the mean.

The three-Gaussian model is also found to be helpful for gaining a better understanding of future temperature variability changes. It is shown that kurtosis changes are mainly dominated by skewness squared changes, which implies that we can understand most of the projected 850-hPa kurtosis changes during winter by simple meridional advection arguments (as these dominate skewness changes). In addition, we show how the three-Gaussian model can be helpful for gaining a simpler interpretation of future temperature variability changes. Specifically, it translates changes in skewness and kurtosis, which are less intuitive, to changes in the averaged magnitude and frequency of cold, near-zero, and warm anomalies relative to the shifted mean, which can be more easily visualized and communicated.

The relation to extremes can be understood as in the following example. In a region with a positively skewed temperature PDF, the three-Gaussian decomposition shows that the mean warm anomalies have a greater magnitude, but occur less frequently than the mean cold anomalies (e.g., Fig. 7f). Nonetheless, because the warm Gaussian is centered around a larger mean value, the warm extremes (at the far right tail of the warm Gaussian) will have a higher likelihood than extreme cold anomalies. In other words, in such a positively skewed region, the mean warm anomalies are stronger and less frequent than the mean cold anomalies, but extreme warm anomalies are both more intense and more frequent.

Similarly, we can consider the future changes in temperature extremes relative to the new mean. For example, if the new mean warm state becomes of greater magnitude but is less frequent than the new mean cold state, the warm extremes could nevertheless become more frequent. Such a region will therefore exhibit a positive skewness change (e.g., middle South America; Fig. 10h). This highlights that the response of the mean warm and cold anomalies can be different from the response of the extremes, and thus care should be taken when considering future changes in warm and cold temperature anomalies.

The model presented here is arguably a good compromise between simplicity and accuracy of representation of the full PDF. It could be made more accurate by allowing the width of the Gaussians to differ between cold, near-zero, and warm anomalies, which would involve more complex mathematical expressions, but could improve the results in terms of recovering the correct PDF shape. While motivated by physical considerations, the simplifying choice $T_0 = 0$ (i.e., that one of the Gaussians is centered around the mean) is another potential limitation of the model, as it forces the equality $p_w T_w = p_c T_c$, which clearly dominates the PDF and its future changes (e.g., it predicts a frequency increase of mean cold anomalies relative to mean warm anomalies in regions where T_c/T_w decreases, such as central-east North America; Fig. 10e). Nonetheless, the remarkable fit between the idealized and raw PDFs (e.g., in Fig. 7 or Fig. 10), as well as the good agreement between the simulated and predicted changes in kurtosis, provides confidence that these are reasonable simplifications. The introduction of additional degrees of freedom would require identifying additional constraints, increasing the danger of overfitting.

Note that some sensitivity to the exact a and b parameters derived from the K versus S^2 scatterplots was found (in some regions, the a and b parameters did not give reasonable results and were therefore discarded). Hence, the exact parameters describing the three Gaussians in each region (i.e., T_w, T_c, p_w, p_c, p_0, and $\hat{\sigma}$) should be taken more qualitatively rather than quantitatively. Adding more data points (e.g., by using ensembles of GCM simulations) could improve the estimated a and b, from which the projected changes in the Gaussians can be derived more accurately. Note also that our results concentrated on DJF, but the three-Gaussian decomposition should also work in other seasons (e.g., June–August) as it does not rely on any special assumptions.

As shown in this work, the third and fourth temperature variability moments (i.e., skewness and kurtosis) are crucial for gaining a complete picture of the underlying PDF. Similarly, the higher-order temperature variability changes must be taken into account for correctly capturing the projected changes in extremes. Future work should further illustrate the role of different processes, such as advection and regional surface feedbacks, in generating these important temperature skewness and kurtosis changes, from which changes in the magnitude and frequency of temperature anomalies can be understood.

Earth System Science Portals. The ERA-Interim data used in this study were obtained from the ECMWF data server: http://apps.ecmwf.int/datasets/.

REFERENCES

Bathiany, S., V. Dakos, M. Scheffer, and T. M. Lenton, 2018: Climate models predict increasing temperature variability in poor countries. *Sci. Adv.*, **4**, eaar5809, https://doi.org/10.1126/sciadv.aar5809.

Bindoff, N. L., and Coauthors, 2013: Detection and attribution of climate change: From global to regional. *Climate Change 2013: The Physical Science Basis*, T. F. Stocker et al., Eds., Cambridge University Press, 867–952.

Brooks, C. E. P., and N. Carruthers, 1953: *Handbook of Statistical Methods in Meteorology*. Met Office, 412 pp.

Cristelli, M., A. Zaccaria, and L. Pietronero, 2012: Universal relation between skewness and kurtosis in complex dynamics. *Phys. Rev. E*, **85**, 066108, https://doi.org/10.1103/PhysRevE.85.066108.

Dai, A., and J. Deng, 2021: Arctic amplification weakens the variability of daily temperatures over northern middle-high latitudes. *J. Climate*, **34**, 5291–2609, https://doi.org/10.1175/JCLI-D-20-0514.1.

David, T. W., D. P. Marshall, and L. Zanna, 2017: The statistical nature of turbulent barotropic ocean jets. *Ocean Modell.*, **113**, 34–49, https://doi.org/10.1016/j.ocemod.2017.03.008.

Dee, D. P., and Coauthors, 2011: The ERA-Interim reanalysis: Configuration and performance of the data assimilation system. *Quart. J. Roy. Meteor. Soc.*, **137**, 553–597, https://doi.org/10.1002/qj.828.

Field, C., and Coauthors, Eds., 2012: *Managing the Risks of Extreme Events and Disasters to Advance Climate Change Adaptation: A Special Report of Working Groups I and II of the Intergovernmental Panel on Climate Change*. Cambridge University Press, 582 pp.

Fischer, E. M., and C. Schär, 2009: Future changes in daily summer temperature variability: Driving processes and role for temperature extremes. *Climate Dyn.*, **33**, 917–935, https://doi.org/10.1007/s00382-008-0473-8.

Gao, Y., L. R. Leung, J. Lu, and G. Masato, 2015: Persistent cold air outbreaks over North America in a warming climate. *Environ. Res. Lett.*, **10**, 044001, https://doi.org/10.1088/1748-9326/10/4/044001.

Garfinkel, C. I., and N. Harnik, 2017: The non-Gaussianity and spatial asymmetry of temperature extremes relative to the storm track: The role of horizontal advection. *J. Climate*, **30**, 445–464, https://doi.org/10.1175/JCLI-D-15-0806.1.

Guszejnov, D., N. Lazányi, A. Bencze, and S. Zoletnik, 2013: On the effect of intermittency of turbulence on the parabolic relation between skewness and kurtosis in magnetized plasmas. *Phys. Plasmas*, **20**, 112305, https://doi.org/10.1063/1.4835535.

Holmes, C. R., T. Woollings, E. Hawkins, and H. de Vries, 2016: Robust future changes in temperature variability under greenhouse gas forcing and the relationship with thermal advection. *J. Climate*, **29**, 2221–2236, https://doi.org/10.1175/JCLI-D-14-00735.1.

Hughes, C. W., A. F. Thompson, and C. Wilson, 2010: Identification of jets and mixing barriers from sea level and vorticity measurements using simple statistics. *Ocean Modell.*, **32**, 44–57, https://doi.org/10.1016/j.ocemod.2009.10.004.

Kodra, E., and A. R. Ganguly, 2014: Asymmetry of projected increases in extreme temperature distributions. *Sci. Rep.*, **4**, 5884, https://doi.org/10.1038/srep05884.

Krommes, J. A., 2008: The remarkable similarity between the scaling of kurtosis with squared skewness for TORPEX density fluctuations and sea-surface temperature fluctuations. *Phys. Plasmas*, **15**, 030703, https://doi.org/10.1063/1.2894560.

Linz, M., G. Chen, and Z. Hu, 2018: Large-scale atmospheric control on non-Gaussian tails of midlatitude temperature distributions. *Geophys. Res. Lett.*, **45**, 9141–9149, https://doi.org/10.1029/2018GL079324.

——, ——, B. Zhang, and P. Zhang, 2020: A framework for understanding how dynamics shape temperature distributions. *Geophys. Res. Lett.*, **47**, e2019GL085684, https://doi.org/10.1029/2019GL085684.

Loikith, P. C., and J. D. Neelin, 2019: Non-Gaussian cold-side temperature distribution tails and associated synoptic meteorology. *J. Climate*, **32**, 8399–8414, https://doi.org/10.1175/JCLI-D-19-0344.1.

Lutsko, N. J., J. W. Baldwin, and T. W. Cronin, 2019: The impact of large-scale orography on Northern Hemisphere winter synoptic temperature variability. *J. Climate*, **32**, 5799–5814, https://doi.org/10.1175/JCLI-D-19-0129.1.

McKinnon, K. A., A. Rhines, M. P. Tingley, and P. Huybers, 2016: The changing shape of Northern Hemisphere summer temperature distributions. *J. Geophys. Res. Atmos.*, **121**, 8849–8868, https://doi.org/10.1002/2016JD025292.

Parey, S., T. T. H. Hoang, and D. Dacunha-Castelle, 2013: The importance of mean and variance in predicting changes in temperature extremes. *J. Geophys. Res. Atmos.*, **118**, 8285–8296, https://doi.org/10.1002/jgrd.50629.

Pearson, K., 1916: IX. Mathematical contributions to the theory of evolution.—XIX. Second supplement to a memoir on skew variation. *Philos. Trans. Roy. Soc. London*, **A216**, 429–457, https://doi.org/10.1098/rsta.1916.0009.

Perron, M., and P. Sura, 2013: Climatology of non-Gaussian atmospheric statistics. *J. Climate*, **26**, 1063–1083, https://doi.org/10.1175/JCLI-D-11-00504.1.

Petoukhov, V., A. V. Eliseev, R. Klein, and H. Oesterle, 2008: On statistics of the free-troposphere synoptic component: An evaluation of skewnesses and mixed third-order moments contribution to the synoptic-scale dynamics and fluxes of heat and humidity. *Tellus*, **60A**, 11–31, https://doi.org/10.1111/j.1600-0870.2007.00276.x.

Ruff, T. W., and J. D. Neelin, 2012: Long tails in regional surface temperature probability distributions with implications for extremes under global warming. *Geophys. Res. Lett.*, **39**, L04704, https://doi.org/10.1029/2011GL050610.

Sardeshmukh, P. D., G. P. Compo, and C. Penland, 2015: Need for caution in interpreting extreme weather statistics. *J. Climate*, **28**, 9166–9187, https://doi.org/10.1175/JCLI-D-15-0020.1.

Sattin, F., M. Agostini, R. Cavazzana, G. Serianni, P. Scarin, and N. Vianello, 2009: About the parabolic relation existing between the skewness and the kurtosis in time series of experimental data. *Phys. Scr.*, **79**, 045006, https://doi.org/10.1088/0031-8949/79/04/045006.

Schär, C., P. L. Vidale, D. Lüthi, C. Frei, C. Häberli, M. A. Liniger, and C. Appenzeller, 2004: The role of increasing temperature variability in European summer. *Nature*, **427**, 332–336, https://doi.org/10.1038/nature02300.

Schneider, T., T. Bischoff, and H. Płotka, 2015: Physics of changes in synoptic midlatitude temperature variability. *J. Climate*, **28**, 2312–2331, https://doi.org/10.1175/JCLI-D-14-00632.1.

Schopflocher, T. P., and P. J. Sullivan, 2005: The relationship between skewness and kurtosis of a diffusing scalar. *Bound.-Layer Meteor.*, **115**, 341–358, https://doi.org/10.1007/s10546-004-5642-7.

Screen, J. A., 2014: Arctic amplification decreases temperature variance in northern mid- to high-latitudes. *Nat. Climate Change*, **4**, 577–582, https://doi.org/10.1038/nclimate2268.

Sura, P., and P. D. Sardeshmukh, 2008: A global view of non-Gaussian SST variability. *J. Phys. Oceanogr.*, **38**, 639–647, https://doi.org/10.1175/2007JPO3761.1.

——, and S. T. Gille, 2010: Stochastic dynamics of sea surface height variability. *J. Phys. Oceanogr.*, **40**, 1582–1596, https://doi.org/10.1175/2010JPO4331.1.

Tamarin-Brodsky, T., K. Hodges, B. J. Hoskins, and T. G. Shepherd, 2019: A dynamical perspective on atmospheric temperature variability and its response to climate change. *J. Climate*, **32**, 1707–1724, https://doi.org/10.1175/JCLI-D-18-0462.1.

——, ——, ——, and ——, 2020: Changes in Northern Hemisphere temperature variability shaped by regional warming patterns. *Nat. Geosci.*, **13**, 414–421, https://doi.org/10.1038/s41561-020-0576-3.

Taylor, K., R. Stouffer, and G. Meehl, 2012: An overview of CMIP5 and the experiment design. *Bull. Amer. Meteor. Soc.*, **93**, 485–498, https://doi.org/10.1175/BAMS-D-11-00094.1.

Volodin, E. M., and A. Y. Yurova, 2013: Summer temperature standard deviation, skewness and strong positive temperature anomalies in the present day climate and under global warming conditions. *Climate Dyn.*, **40**, 1387–1398, https://doi.org/10.1007/s00382-012-1447-4.

Xu, Z., F. Huang, Q. Liu, and C. Fu, 2020: Global pattern of historical and future changes in rapid temperature variability. *Environ. Res. Lett.*, **15**, 124073, https://doi.org/10.1088/1748-9326/abccf3.